Numerical and experimental investigation of gas powder flow from coaxial nozzles in Laser Metal Deposition

E. Ferreira[1,2,3], M. Dal[2], P. Peyre[2], C. Colin[3], G. Marion[1], D. Courapied[1], B. Macquaire[1]
[1] Safran, Paris Cedex 15, France
[2] PIMM Laboratory, UMR 8006 ENSAM – CNRS – CNAM, 75013 Paris,
[3] France Centre des Matériaux, UMR 7633 MINES Paris Tech, 91100 Evry, France

Abstract: Laser Metal Deposition (LMD) is an additive manufacturing process able to produce, repair and add coatings or functions to 3D metallic parts. During the process, a filler material – such as powder particles – is injected through a design nozzle into a melt pool generated by the interaction of a laser beam on a metallic substrate surface. The powder stream is a key component of the process but its dependence with the nozzle design and the carrier and protective gases jets makes it difficult to control and master. The present work is focused on the understanding of the behavior of the multiple gas jets flowing through three different nozzles and on the impact of the latter's design. To achieve this work, a CFD turbulent model as well as TDS (Transport of Diluted Species) laminar model with Particle Tracing module were developed using COMSOL Multiphysics software. Results show the influence of nozzle design, gas flow rate and outside atmosphere on the gas jet velocity and vortices appearance during the process. To confirm the numerical gas structure and velocity, an experimental setup based on a pitot tube local velocity measurement were conducted. Comparison show a good correlation between numerical and simulated gas behavior.

Keywords: Laser cladding, Direct Metal Deposition, Coaxial nozzle, Gas flow, Experimental setup, Pitot probe

1. Introduction

Laser Metal Deposition (LMD) process is an additive fabrication method which provides a possibility to produce new net shape metallic components and that can be used as a repair technology for damaged parts [1]. It is composed by multiple gas streams flowing inside a deposit nozzle to shape a powder jet, which feeds a molten pool created by the interaction of a focused laser beam on a metallic substrate [Fig. 1]. In the recent years, LMD was increasingly developed in multiple manufacturing industries. However, despite the improvements, the accuracy, quality and reliability of the cladding system largely depend on a considerable number of parameters and their interactions are not always well understood and controlled [2]. The powder stream is a key factor governing the laser cladding process, but its structure, focal plan and distribution is partly tailored by the nozzle geometry and gas flow rate [3], [4].

Previous works dealing with the two-phase flow modelling of the gas-powder stream usually consider a one-way coupling, meaning that the impact of the gas phase on the particle stream is considered while the influence of the powder phase on the gas jet is neglected [5]–[8]. Therefore, to understand and master the powder stream, and then the LMD deposit, it is first necessary to ensure a strong gas modelling. In this study, investigation of the gas flow behavior is performed using a turbulent CFD numerical model. To ensure its reliability, this study was conducted on three different nozzle designs and was compared to experimental data from a local fluid flow velocity measurement setup. Finally, Transports of Dilutes Species and Particle Tracing modules were performed to understand and control the impact of an air-based external area on the gas and powder stream.

2. LMD machines and nozzles

Three coaxial nozzles (A, B and C), with two laser cladding machines, were used for this work. The particularity of a coaxial nozzle is the creation of a focused axisymmetric gas-powder flow in the laser beam direction. Each deposit nozzle possesses its own design and its own set of parameters.

The first cladding machine is a 5 continuous axis machine equipped with two removable nozzles heads according to the size of the needed deposit. The first one, "*nozzle A*", is the smallest nozzle head of the study. It

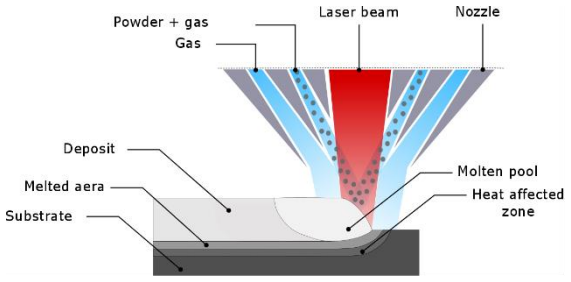

Figure 1 : schematic of the LMD process

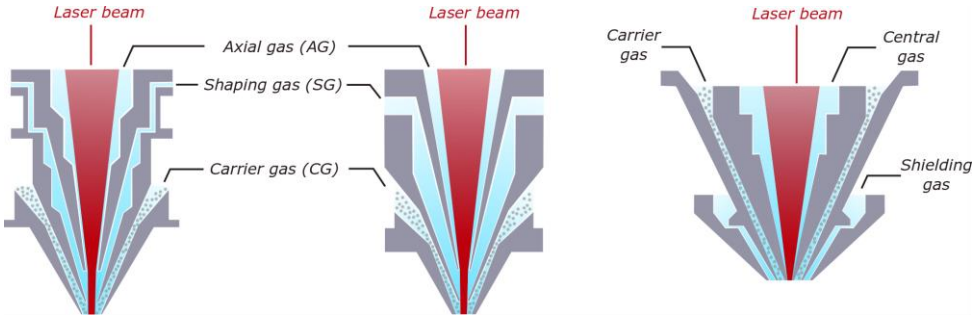

Figure 2 : schematics of : a. nozzle A, b. nozzle B, c. nozzle C

allows a width deposit of 0.8 to 1.2 mm and needs a 3.5mm standoff distance during the process. The second nozzle, called *"nozzle B"*, allows a thicker deposit, usually between 2 to 2.4 mm, and works with a 13mm standoff distance. As for design, the nozzle are composed of 3 conic extensions [Fig. 2.a, b] leading to three gas channels: an axial channel – where an axial gas (AG) is propagated to protect the laser beam optics –, a middle annular channel – with a shaping gas (SG) which gives the powder stream's structure –, and an external annular channel where a carrier gas (CG) hold the particle inside the nozzle until they get to the shaping flow.

The second machine is an instrumented test bench equipped with a laboratory made coaxial deposit head (*"nozzle C"*). The latter is composed of 2 cones where distinct flows go through: central (CG) and carrier gas (CG) [Fig. 2.c]. A supplementary third cone, along with a shielding gas, can be added to improve the gas shielding and to compress and envelopes the powder stream.

In both cases, each flow injected in the deposit heads is an inert gas (argon).

3. Gas flow simulation in an inert atmosphere

In a first stage, a numerical modelling of the gas streams flowing inside the deposit nozzle to an external atmosphere with same gas properties is proposed. The inert external atmosphere assumption makes the simulation more convenient compared to the implementation the mixture of two gases (inert and air-based) below the nozzle and is more suitable to most real deposit cases. The gas is set with pure argon properties (ρ = 1.78 kg/m^3, μ = 2.09 10^{-5} Pa.s) and is supposed Newtonian. Moreover, assuming that the gas velocity won't exceed 0.3Ma at the nozzle's outlets, the flowing gas is supposed incompressible.

3.1. Geometric modelling and meshing

Regarding the conical shape of the studied nozzles, a 2D axisymmetric model was developed to simulate and study the gas flow behavior inside and below them. The scheme of the computational domain includes the internal geometry of the nozzle channels and cylindrical computation area (Φ=30mm * L=30mm) built to visualize the gas flow behavior below the nozzle tips. This domain was meshed with triangular elements with a decreasing size near the corners of each nozzle.

3.2. Governing equations

As the Reynolds number of the flows is quite high (at least 1000, according to the nozzle) a turbulent model must be considered. Moreover, to reduce the computation type and assuming that the unsteadiness in the flow and the flow itself can be treated separately ($u_i = u_i + u_i'$), the RANS (Reynolds Average Navier-Stokes) models seems to be a convenient choice. Thereby, for an incompressible flow, the turbulent model can be described by the 2 main equations below [9]:

Conservation of mass:

$$\rho \nabla \cdot (u) = 0 \quad \textbf{(1)}$$

Conservation of momentum (Navier-Stokes):

$$\rho \frac{\partial u}{\partial t} + \rho(u \cdot \nabla)u = \nabla \cdot \left[-pI + (\mu + \mu_T)\left(\nabla_u + \nabla_u{}^T\right)\right] \textbf{(2)}$$

where u is the mean velocity vector, p is the pressure, ρ is the gas density, μ is the dynamic viscosity and μ_T is the dynamic viscosity of the gas.

At this point, means values of velocity and pressure can only solve these equations if the Reynolds stress tensor can be derived in some way. Therefore, the temporal and spatial evolution of the gas flow needs to be specified by new equations in a time average manner. Those can be provided by diverse turbulence models, whose most commonly used is a two-equations model known as the k-ϵ [9]–[11]. In this case, the turbulence field is characterized by the kinetic energy k and the viscous dissipation rate of the turbulent kinetic energy ϵ. With a sequence of algebraic equations, two transport equations can be obtained from the Navier-Stokes as follow:

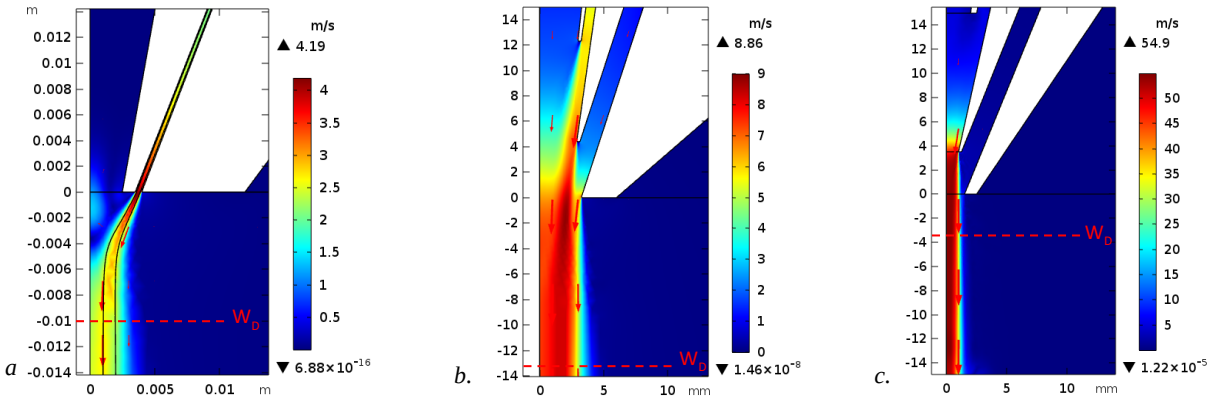

Figure 3: gas behavior obtained for: a. nozzle C with D_{AG} = 0.1 L/min and D_{CG} = 4 L/min; b. nozzle B with D_{AG} = 3L/min, D_{SG}=6L/min and D_{CG} = 5L/min; c. nozzle A with D_{AG} = 3L/min, D_{SG}=6L/min and D_{CG} = 3L/min

Conservation of the kinetic energy of turbulence:

$$\frac{\partial}{\partial x_j}(\rho \bar{u}_j k) = \frac{\partial}{\partial x_j}\left(\frac{\mu_t}{\sigma_k}\frac{\partial k}{\partial x_j}\right) + G_k + G_b - \rho\varepsilon \quad \textbf{(3)}$$

Conservation of the dissipation of kinetic energy of turbulence:

$$\frac{\partial}{\partial x_j}(\rho \bar{u}_j \varepsilon) = \frac{\partial y}{\partial x_j}\left(\frac{\mu_t}{\sigma_\varepsilon}\frac{\partial \varepsilon}{\partial x_j}\right) + C_1 \frac{\varepsilon}{k}(G_k + G_b) - C_2 \rho \frac{\varepsilon^2}{k} \quad \textbf{(4)}$$

$$G_k = \mu_t \frac{\partial \bar{u}_i}{\partial x_j}\left(\frac{\partial \bar{u}_i}{\partial x_j} + \frac{\partial \bar{u}_j}{\partial x_i}\right) \quad \textbf{(5)}$$

$$G_b = -g_i \frac{\mu_t}{\rho P_{r_t}} \frac{\partial \rho}{\partial x_i} \quad \textbf{(6)}$$

$$\mu_t = \frac{\rho C_\mu k^2}{\varepsilon} \quad \textbf{(7)}$$

where i,j = 1,2,3, $\mu = \mu_0 + \mu_t$ (with μ_0 the molecular viscosity and μ_t the turbulent viscosity from Kolmogorov-Prandlt). $C_1, C_2, \sigma_\varepsilon, \sigma_k$ *and* C_μ are empirical constant optimized by the years as follow: C_1, = 1.44, C_2= 1.92, σ_ε = 1.3, σ_k = 1.0, C_μ = 0.09 [COMSOL 5.3a]. G_k and $G_b$represent respectively the rate of production of kinetic energy and the generation of turbulence, P_{r_t} is the turbulent Prandtl number of energy.

3.3. Boundary settings

To numerically solve the turbulent Navier-Stokes equation system, the initial pressure is set to $P_0 = 1.10^5$ Pa and the initial temperature T_0 = 293 K. As for the gas initial condition, the flow rate of the carrying, central and shaping gas were pre-set at the channels input of each nozzle. A standard no-slip condition was assigned on the nozzle walls and the outlet of the computational domain was treated as a pressure outlet of 1.10^5 Pa [4, 5] and a disappearance condition was used.

3.4. Results and discussion

[Fig. 3] show the pattern and velocity progression of the gas flow inside the coaxial channels of the studied nozzles and in their external area. Due to its very low input flow rate, the axial gas coming from *nozzle C* doesn't seem to have a real impact on the process. However, the carrier gas undergoes a significant acceleration, caused by the convergent shape of its channel, and reaches a maximum velocity of 4.2 m/s at its outlet tip. From this point, the gas stream decelerates in the inert atmosphere of the external area and reaches 1.5 m/s at its working distance (10mm). As for *nozzles A* and *B*, it is shown that the jets flowing at their outlets are created from the combination of axial and both annular channels gas streams. A 55 and a 9 m/s maximum velocity are respectively generated at nozzles A and B outlets and neither gas jet seems to decelerate as fast as the one created by *nozzle C*. If the significant velocity increase generated by *nozzle A* can be explain by its very thin gas channel outlets – which are three times lower than with *nozzle B* –, this result doesn't seem realistic and must be used with precautions. Indeed, such a flow rate could have a considerable impact on the melting pool formation, shape and stability.

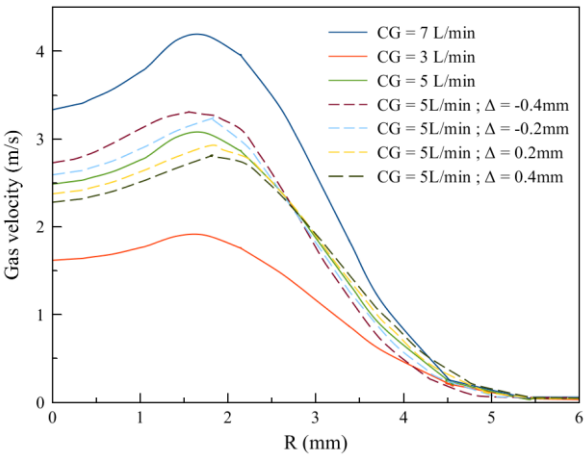

Figure 4: influence of nozzle B's carrier gas flow rate and channel diameter on its outlet gas velocity

From these results, it is clear that the nozzle design, number of gas channels and their respective flow rate have a considerable impact on the gas flow of the process and, therefore, on the powder stream. Moreover, a sensitivity study of those parameters showed that an increase of the gas flow rate as well as a slight decrease of one channel diameter lead to a considerable rise of the gas velocity [Fig. 4].

4. Experimental validation of fluids structure and velocity

For this study, the gas flow was monitored with an intrusive velocity measurement instrument known as a pitot tube. It is a differential pressure anemometer that allows the velocity measurement of a single localized fluid flow [13]. Such a device is made of a tube with an open end facing the fluid flow (total pressure entrance) and of an orifice flush tangential to the tube, which register the static pressure [14]. The pressure difference between total and static entrance is operated on the basis that the fluid kinetic energy is converted to an increase of pressure when the fluid comes to rest at the Pitot tube tip. Under most conditions, the drop of pressure between the two orifices can be converted into velocity by Bernoulli's equation [15]:

$$v = \sqrt{\frac{2\,\Delta P}{\rho}} \quad (8)$$

where ρ is the fluid density and ΔP the pressure difference measure by the pitot tube. Due to its low cost, its compactness and its ease of installation, pitot tubes are used in many industrial fields to measure or control fluid flows. However, their accuracy can be limited when an unsteady flow is studied, especially when the viscous effects becomes too significant (low Reynolds number). Studies conducted by [13] and [16] showed that pitot measurement conducted with a Reynolds number lower than 100 could not be accurately predicted with Bernoulli's method and needs correlation terms to correct it. In this study, the Reynolds numbers of each gas flow from the 3 studied nozzles are higher than 1000, meaning that basic Bernoulli's equation is enough to describe the speed flow.

4.1. Experimental setup

A pitot tube with an entrance diameter d = 0,5 mm and an internal diameter D = 2 mm was used with sensors of 125 and 500Pa according to the studied nozzle. Before the experiment, the pitot instrument is arranged along the nozzle direction and sets perpendicularity to the working table with a set square. The centering adjustment between the tube and the nozzles was realized with the coaxial camera of the machine and the standoff distance between the nozzle and the tube tip was controlled with gauge blocks.

Since a single measurement couldn't be enough to describe the entire gas flow velocity field of the process, multiple measurements following a 2D grid of 3*3 to 4*4 mm² was programmed. During the experiment, the Pitot tube (or the nozzle head) moves of 0.25mm along the X and Y axis to reach each point of the grid and stops for few seconds to continuously register data with a Raspberry Pi nano-computer [Fig. 5.a]. Results were obtained from an average on a 7s acquisition with a 0.5s delay after each axis displacement to ensure the acquisition stability. The result maps were then interpolated with a bilinear function [Fig. 5.b-d].

4.2. Results and discussion

The result maps obtained show the velocity variation of the gas jet created by the deposit nozzles along the X and Y axis. First, the geometrical shape obtained 1 mm below *nozzle C* tips [Fig. 5.b] indicates that the Pitot tube doesn't seem to interfere with the jet gas, which has been confirmed by numerical simulations. Then, the comparison of velocity maps obtained at multiple plans allows tracing the gas jet caustics. Results obtained from *nozzle C* show the structure variation of the gas jet during its trajectory in the air-based atmosphere at 1 [Fig. 5.b] and 10 mm [Fig. 5.c] below the nozzle tips. Because of the convergent shape of its pathway and the low influence of its axial gas, the jet structure is first annular and becomes more convergent with distance from the nozzle tips. A nearly uniform jet is obtained around the nozzle working distance, which confirm the simulated jet structure previously obtained. As with its simulations, results from *nozzle A* and *B* experiments show a more uniform gas jet structure along its trajectory due to their important axial and shaping gas flow rates. For each nozzle working distance, gas jets diameters reached about 3 mm for *nozzle A*, 7 mm for *nozzle B* and 5mm for *nozzle C*, which still confirm previous simulations

Regarding the gas velocity, multiple experimental tests were conducted to consider several gas flow rates and active gas channels conditions. For all cases, simulations always seem to overestimate the gas velocity with a 1.1 to 2.6 correlation factor. This gap between experimental and simulation results can be related to an insufficient calibration of the Pitot tube, which will be investigated in further works. Despite this calibration gap, the experimental setup reveals the considerable velocity difference between *nozzle A* and *nozzles B and C* previously predicted by simulation [Table 1].

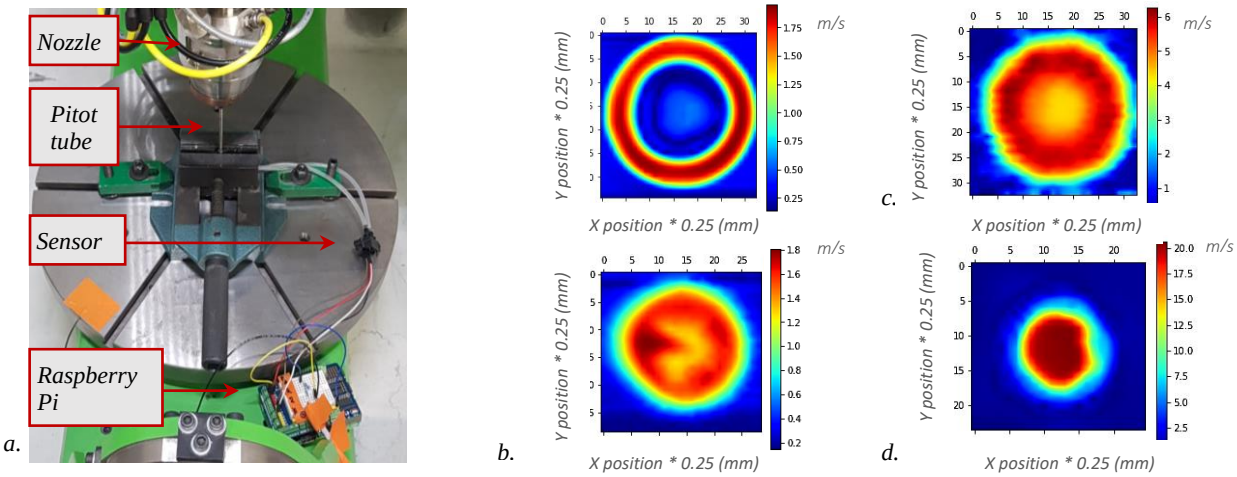

Figure 5: a. experimental setup; b. experimental velocity maps (m/s) obtained at 1 mm and 10 mm below nozzle C; c. experimental velocity maps (m/s) obtained at 13 mm below nozzle B and d. at 3.5mm below nozzle A

Since previous simulations assumed an inert external area while the experimental setup was conducted in an air-based atmosphere, part of the experimental-simulation results gap could be explained by the interaction of the two gases below the nozzles. Indeed, experimental visualization of the gas structure performed with schlieren imaging by [17] revealed the formation of instabilities between the injected inert gas jet and an air-based atmosphere. These instabilities, which become greater with an increase of the gas flow, can destabilize the gas jet and deflect a substantial part of the powder jet off the weld zone, leading to a decrease in the process productivity. To ensure the validity of previous simulations and make sure there is no influence of the air-based atmosphere on the gas jet or the powder stream, new numerical works were conducted.

Nozzle design	A	B	C
Experiment (m/s)	10	5.5	1.5
COMSOL model (m/s)	55	8.5	2.5

Table 1: comparison of maximum gas velocity obtained with numerical and experimental data for the three studied nozzles

5. Gas flow simulation in an air-based atmosphere

To visualize the interactions between the injected inert gas stream (argon) in the air-based atmosphere, a numerical modeling based on the combination of CFD and Transport of Diluted Species (TDS) modules is proposed. To ease the resolution time of the simulation and to take the gas change into account, a compressible laminar gas flow is supposed. Moreover, the particle tracing module was performed to understand the gas flow influence on the powder stream trajectory and velocity.

5.1. Governing equations

The mixture of the two gases below a deposit nozzle can induce a concentration gradient and lead to convection and diffusion effects. To understand and visualize the concentration evolution between these two species and their interaction, it is necessary to consider the convection-diffusion equation:

$$\frac{\partial c_i}{\partial t} + \nabla \cdot \left(-D_i \nabla_{c_i}\right) + u \cdot \nabla c_i = Ri \quad (9)$$

$$Ni = -D_i \nabla c_i + u_{c_i} \quad (10)$$

where D_i is the diffusion coefficient, which is set constant to 1.10^{-9} m²/s, c_i is the seek concentration of the gas flow, and u is its velocity. The latter is simultaneously calculated based on the laminar model with the compressible Navier-Stokes equations below:

Conservation of mass:

$$\frac{\partial \rho}{\partial t} + \nabla \cdot (\rho u) = 0 \quad (11)$$

Conservation of momentum (Navier-Stokes):

$$\rho\left(\frac{\partial u}{\partial t} + (u \cdot \nabla_u)\right) = -\nabla_p + \nabla \cdot \left(\mu\left(\nabla u + \nabla u^T\right)\right) - \frac{2}{3}\mu(\nabla \cdot u) + F \quad (12)$$

where u is the gas velocity, p is the gas pressure, ρ is the gas density and μ is the gas dynamic viscosity.

The powder stream trajectory and velocity were performed based on the following assumptions:

- collision between particles and particles effect on the gas phase were neglected due to their low volume fraction (<10%) [10]
- only gravity and drag forces were considered
- particles were considered spherical, but their size was defined by a realistic distribution (Gaussian) with d_{10} = 45 and d_{90} = 105 µm
- IN718 particles (ρ = 8190 kg.m^{-3}) with a mass flow rate of 4 g/min were considered.

5.2. Boundary conditions

In the TDS module, the density of the geometric domain is set to the density mixture equation below:

$$\rho_{mix} = c\,\rho_1 + (100 - c)\,\rho_2 \quad (\mathbf{13})$$

with ρ_{mix} the air-argon mix density, ρ_1= 1.78 kg/m^3 the argon density, ρ_2 = 1.2 kg/m^3 the air density and c the seek argon concentration. Based on this equation, the gas inputs and their respective channels are set to an initial condition of c = 100% – to consider an argon-based atmosphere – while the under-nozzle area is set to an initial value of c = 0% to consider an air-based medium. As for the nozzle walls, a standard no-slip condition was assigned, and the outlet of the computational domain was set to a disappearance condition with P = P_0.

For the powder stream, interaction with nozzle walls and the symmetry axis were considered as elastic rebound and a disappearance condition was set at the outlet of the computational domain.

5.3. Results and discussion

Argon stream behavior of *nozzle C* in the air-based atmosphere is represented on [Fig. 6.a]. The flow behavior below the deposit nozzle isn't as stable as the one observed with a simple turbulent model in an inert atmosphere. Numerical results show the appearance of growing vortices across the interface of argon and air environment. This observation can be linked to the Kelvin-Helmholtz instability which occurs when a velocity shear exists at the interface of two fluids with different densities. This velocity discontinuity induces vorticity at the interface and produce an unstable vortex sheet that rolls up into a spiral [18]. The Kelvin-Helmholtz instability is developed when the Richardson number (Ri) is less than 0.25 [19]:

$$Ri\,(z) = \frac{g\,(\rho_2 - \rho_1)}{\rho_1\,(v_1 - v_2)} \quad (\mathbf{14})$$

where g is the gravitational force, ρ the fluid densities and u its velocity. Regarding the velocity field previously obtained by numerical computation with 3 gas inlets, the Richardson number reaches 0.2, which justify the observed instabilities.

Same work was applied on *nozzle B* at its usual gas flow rate [Fig. 6.b]. Despite its low Richardson number of 0.03, no vortex seems to appear at the interface of the gas mixture. This result can be linked to the higher gas flow rate of *nozzle B* which can lead to an increase of the stable length (before appearance of instabilities) making the instabilities appear outside of the simulated domain. Regarding the gas velocity result from part 3., we can consider that same vortices behavior can be induce by *nozzle A*.

For both cases, the most critical vortices appear below the commonly working distance used with both nozzles during process ($W_{D,\,nozzle\_C}$ = 10mm, $W_{D,\,nozzle\_B}$ = 13mm) and doesn't have an influence on the gas velocity calculated with previous inert atmosphere model. Moreover, results from *nozzle C* show that the particle stream isn't affected by the low vortices at its working distance [Fig. 7]. Therefore, we can consider that the air-based external atmosphere doesn't have an impact on the gas and particle stream of the LMD process as long as the nozzle working distances are respected.

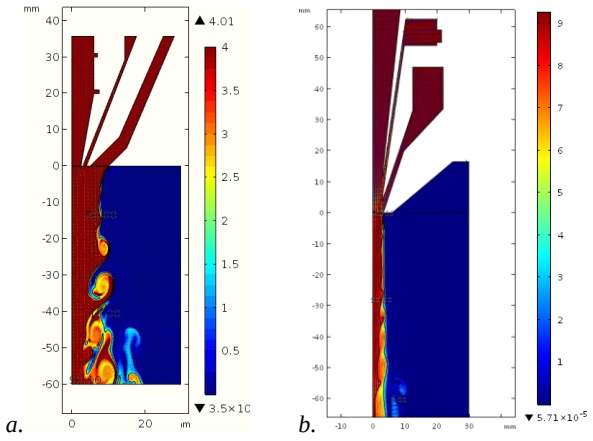

Figure 6: argon concentration behavior for: a. nozzle C and b. nozzle B

Regarding the particle behavior, [Fig. 7] shows the continuous acceleration of the powder inside the nozzle channel. Compared to the gas behavior, particles continue to accelerate below the nozzle and reach their maximum value of 1.2 m/s after their focal position. If the maximum particles velocity only reaches 0.3 times the gas velocity, both focal plans are located around 10mm below the nozzle tips. After this position, two set of particles behaviors appear: the lighter particles, i.e. the smaller ones, are faster and follow the gas trajectory, whereas the heavier ones, i.e. the bigger particles, are slower and follow their own path. These observations need to be confirmed with further experimental works.

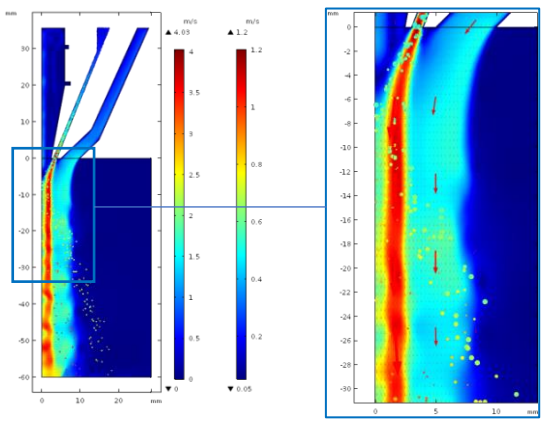

Figure 7: gas and particle behavior below nozzle C

6. Conclusion

Analysis of the fluid behavior by means of simulations and experimental data was carried out to improve the understanding of the LMD process. Typical patterns of the gas flow inside and below three types of coaxial nozzles were conducted using COMSOL Multiphysics software.

A turbulent incompressible CFD model first showed the considerable impact of the nozzle design, gas flow rate and number of gas channels on the external structure and velocity field of the gas stream in an inert atmosphere. Structure of the gas flows as well as the influence of the flow rate parameter and the design of the nozzle were confirmed by pitot tube experimental setup, but a 1.1 to 2.5 correlation factor appeared between experimental and simulated gas velocities. This gap is mainly explained by an insufficient calibration of the pitot tube, which will be studied in further works. The TDS laminar model proved that the air-based external atmosphere doesn't need to be considered to estimate the gas behavior since the vortex's instabilities appeared much lower than the usual working distance of the studied nozzles and don't impact its velocity field. Finally, particle tracing result showed the influence of the particle diameter in the powder stream trajectory and velocity: the heavier the particles, the faster they are and more they follow the gas path.

References

[1] R. M. Mahamood, "Introduction to Laser Metal Deposition Process," *Laser Met. Depos. Process Met. Alloy. Compos. Mater. , Eng. Mater. Process.*

[2] A. Lamikiz, J. I. Arrizubieta, E. Ukar, S. Martínez, J. E. Ruiz, and M. Cortina, "Numerical approach for the estimation of the deposited material on the laser material deposition process," *Procedia CIRP*, vol. 74, pp. 785–789, 2018.

[3] J. Lin, "Numerical simulation of the focused powder streams in coaxial laser cladding," *J. Mater. Process. Technol.*, 2000.

[4] J. Maisonneuve, "Fabrication directe de pièces aéronautiques en ta6v et in718 : projection et fusion sélective par laser," 2008.

[5] S. Y. Wen, Y. C. Shin, J. Y. Murthy, and P. E. Sojka, "Modeling of coaxial powder flow for the laser direct deposition process," *Int. J. Heat Mass Transf.*, 2009.

[6] B. Zhang and C. Coddet, "Numerical study on the effect of pressure and nozzle dimension on particle distribution and velocity in laser cladding under vacuum base on CFD," *J. Manuf. Process.*, 2016.

[7] I. Kovaleva, O. Kovalev, A. V. Zaitsev, and D. V. Sergachev, "Modeling and numerical study of light-propulsion phenomena of particles acceleration in coaxial laser powder cladding," in *Physics Procedia*, 2014.

[8] S. Morville, "Modélisation multiphysique du procédé de Fabrication Rapide par Projection Laser en vue d'améliorer l etat de surface final," Université de Bretagne Sud, 2013.

[9] S. Zekovic, R. Dwivedi, and R. Kovacevic, "Numerical simulation and experimental investigation of gas-powder flow from radially symmetrical nozzles in laser-based direct metal deposition," *Int. J. Mach. Tools Manuf.*, 2007.

[10] J. L. Arrizubieta, I. Tabernero, J. Exequiel Ruiz, A. Lamikiz, S. Martinez, and E. Ukar, "Continuous coaxial nozzle design for LMD based on numerical simulation," in *Physics Procedia*, 2014.

[11] I. O. Kovaleva and O. B. Kovalev, "Simulation of the acceleration mechanism by light-propulsion for the powder particles at laser direct material deposition," *Optics and Laser Technology*. 2012.

[12] O. B. Kovalev, I. O. Kovaleva, and I. Y. Smurov, "Numerical investigation of gas-disperse jet flows created by coaxial nozzles during the laser direct material deposition," *J. Mater. Process. Technol.*, 2017.

[13] R. B. Spelay, F. Adane, R. S. Sanders, R. J. Sumner, and R. G. Gillies, "The effect of low Reynolds number fl ows on pitot tube measurements," vol. 45, pp. 247–254, 2015.

[14] S. Chevula, Á. Sanz-Andres, and S. Franchini, "Estimation of the correction term of pitot tube measurements in unsteady (gusty) flows," *Flow Meas. Instrum.*, vol. 46, pp. 179–188, 2015.

[15] V. Vinod, T. Chandran, G. Padmakumar, and K. K. Rajan, "Calibration of an averaging pitot tube by numerical simulations," *Flow Meas. Instrum.*, vol. 24, pp. 26–28, 2012.

[16] S. K. S. Boetcher and E. M. Sparrow, "Limitations of the standard Bernoulli equation method for evaluating Pitot/impact tube data," *Int. J. Heat Mass Transf.*, vol. 50, no. 3–4, pp. 782–788, 2007.

[17] K. Y. Nagulin, F. R. Iskhakov, A. I. Shpilev, and A. K. Gilmutdinov, "Optical diagnostics and optimization of the gas-powder flow in the nozzles for laser cladding," *Opt. Laser Technol.*, 2018.

[18] V. A. Smalyuk *et al.*, "Measurements of turbulent mixing due to Kelvin-Helmholtz instability in high-energy-density plasmas," *High Energy Density Phys.*, vol. 9, no. 1, pp. 47–51, 2013.

[19] P. G. Drazin, "Dynamical Meteorology: Kelvin-Helmholtz Instability," *Encycl. Atmos. Sci. Second Ed.*, vol. 3, pp. 343–346, 2014.